Article

Fabrication of porous beta-cyclodextrin functionalized PVDF/Fe–MOF mixed matrix membrane for enhanced ciprofloxacin removal

Check for updates

Lewis Kamande Njaramba[1], Yeomin Yoon[2] & Chang Min Park [1] ✉

Herein, we demonstrate the synthesis of beta-cyclodextrin (β–CD) functionalized polyvinylidene fluoride (PVDF) and iron-based metal-organic framework (Fe–MOF) mixed matrix membrane (MMM) for the enhanced removal of ciprofloxacin (CIP) from water. The membranes were prepared using the phase inversion technique with PVDF as the polymer matrix, Fe–MOF as the filler, and polyvinylpyrrolidone (PVP) as the porogen. The optimized MMM with 7% wt. Fe–MOF exhibited excellent performance with 87.6% removal efficiency. Moreover, the maximum adsorption capacity was 6.43 mg g^{-1}. The β–CD functionalization improved the MMM hydrophilicity exhibited by the water contact angle (WCA) analysis (WCA = 55°). Furthermore, excellent adsorption performance can be attributed to the large Fe–MOF specific surface area (682.5 m^2 g^{-1}), the high porosity (77%), and the average pore diameter (395 nm) of the membrane. The inclusion of PVP (1% wt.) enhanced the porous nature of the MMM and, consequently, the adsorption performance for CIP. Notably, the hydrophilic and macroporous membrane showed good reusability with over 70% removal efficiency after five sequential adsorption–desorption cycles. The insights from this study suggest that the PMC–7 membrane can be an excellent candidate for the remediation of organic contaminants from aquatic environments.

Antibiotics are a class of drugs that are extensively prescribed in both human and animal healthcare for the prevention and treatment of disease and infection. Ciprofloxacin (CIP) is a second-generation fluoroquinolone antibiotic whose widespread use and inappropriate disposal have caused global concern due to its persistent release and bioaccumulation in the environment, posing a threat to both human and aquatic life[1,2]. Various studies have identified CIP and its metabolites in groundwater, surface runoff, wastewater, and even drinking water at varying concentrations[3]. Diverse approaches and technologies have been explored for the removal of CIP in different environmental matrices, such as adsorption, biodegradation, advanced oxidation processes, membrane separation, and electrochemical degradation[4–8]. Adsorption is a widely used process due to its ease of operation, inexpensive, versatility, simplicity, and great efficacy[9].

Metal-organic frameworks (MOFs) are porous crystalline materials made up of metal clusters and organic linkers coupled together by coordination bonds. MOFs have been rapidly developed and studied in the removal of organic pollutants due to their attractive attributes, namely large specific surface area (SSA), multiple reaction sites, thermal, and chemical stability[10,11]. In particular, NH$_2$-MIL-88B (Fe–MOF) is one of the most studied iron (Fe) based MOFs as adsorbents for organic contaminants[12]. The Fe–MOF has plentiful hydrogen-rich organic ligands and amino groups, which further aid the compatibility with the other molecules via hydrogen bonds and covalent bonding. Fe-based MOFs have desirable characteristics and versatility and have found use in various applications[13]. Moreover, the majority of the Fe–MOFs have good stabilities in organic solvents and water. However, the use of MOF powders in wastewater treatment faces adverse challenges such as poor separation and processability, powder agglomeration, and recyclability. To overcome these challenges, it is imperative to explore different polymer substrates to compound MOFs and improve their adsorption, separation, and stability performance.

[1]Department of Environmental Engineering, Kyungpook National University, 80 Daehak-ro, Buk-gu, Daegu 41566, Republic of Korea. [2]Department of Environmental Science and Engineering, Ewha Womans University, 52 Ewhayeodae-gil, Seodaemun-gu, Seoul 03760, Republic of Korea. ✉e-mail: cmpark@knu.ac.kr

Polyvinylidene fluoride (PVDF) polymer has been widely used in membrane synthesis due to its low cost, chemical, thermal, and mechanical stability. This makes it an ideal substrate choice for immobilizing functional materials such as MOFs and, thus, the preparation of mixed matrix membranes (MMM). The mixed-matrix concept combines the merits of porous fillers such as MOFs into the processable polymeric matrix that aids in overcoming the separation challenges and synergistically enhancing the performance of the MMM[14,15]. Furthermore, different approaches have been explored to enhance the adsorptive efficacy of PVDF-based membranes, including surface coating, grafting, copolymerization, and blending[16–18]. Furthermore, the membrane morphology and performance can be altered by controlling its hydrophilicity and porosity. Surface modifications of polymeric membranes through covalent and non-covalent interactions have been shown to improve the adhesion of fillers as well as reduce unwanted agglomerations to improve their performance[19]. Cyclodextrin (CD) is a water-soluble cyclic oligosaccharide composed of multiple glucose units coupled by α-(1-4) glycosidic linkages. Beta-cyclodextrin (β–CD) is capable of host-guest interactions with organic contaminants due to its truncated cone shape, which contains a hydrophobic inner cavity (C–O–C and C–H bonds) and a hydrophilic outer surface (primary and secondary hydroxyl groups)[20]. Moreover, β–CD is environmentally benign, biodegradable, non-toxic, and inexpensive. In addition, it is rich in hydroxyl functional groups that can serve as coordination sites to effectively form complexes with organic contaminants. β–CD-based materials have attracted wide attention in the environmental remediation of various organic pollutants[14,21,22]. Pore-forming additives (porogens) such as polyvinylpyrrolidone (PVP) are frequently added to improve the porosity and permeability of membranes. PVP has diverse functional groups that promote surface modifications and dispersion of nanofillers in the polymeric matrix[23]. In this study, PVP was employed to induce the enlargement of the macropores in the membrane and thus facilitate the adsorption process.

Machine learning (ML) prediction tools, including random forest, adaptive neuro-fuzzy inference system (ANFIS), least square support vector regression (LSSVR), and artificial neural network (ANN) have been widely employed in various applications in the field of wastewater treatment[24–26]. Particularly, ANN has gained tremendous attention in the different environmental remediation processes in the attempt to elucidate and develop the complex and nonlinear relationships between input and output variables due to its adaptability, simplicity, nonlinearity, reliability, and flexibility[27]. Moreover, ANN models have been applied in the assessment, performance prediction, and optimization for the removal of various organic pollutants[28–30]. However, the use of ANN in the modeling and performance evaluation of MMM adsorbents for the removal of antibiotics remains largely unexplored.

Different types of membranes have been developed for the removal of CIP. For example, Qalyoubi et al.[31] reported an adsorptive membrane using polyether sulfone and zirconium phosphate for the removal of CIP. However, the high removal efficiency was achieved using both adsorption and membrane filtration processes. Das et al.[32] prepared an electrospun cellulose acetate-based membrane for the removal of CIP and reported a 76% removal efficiency. Guo et al.[33] prepared a PVDF membrane for the removal of CIP using membrane distillation, with almost 100% removal efficiency. Bhattacharya et al.[34] developed an ultrafiltration membrane using copper oxide and titanium dioxide nanoparticles supported over clay/alumina for the removal of CIP. They reported 99% removal within 60 min. However, the use of membrane-based technologies for the removal of antibiotics faces challenges such as membrane fouling and are usually pressure-driven processes[35]. Despite the successes in the preparation of MMMs, they have been rarely reported for their adsorptive removal of antibiotics. With this in mind, we designed a simple and efficient β–CD surface functionalized PVDF-MOF MMM adsorbent. The novelty of this study was the development of a facile technique for the construction of a β–CD surface functionalized PVDF-MOF MMM adsorbent for the enhanced removal of CIP. The composite MMM properties, such as porosity, water contact angle (WCA), morphology, and thermal stability were studied in detail. In addition, ANN modeling using four input variables (time, pH, temperature, and mass) and two output variables (adsorption capacity and removal efficiency) was developed to predict the removal of CIP. Finally, the adsorption performance of MMM, reusability, and the effect of various effects such as pH, coexisting ions, and contact time on its performance were studied and discussed.

Results and discussion
Characterization of the prepared membranes
Figure 1a exhibits the X-ray diffraction (XRD) pattern of Fe–MOF, β–CD, PM–7, and PMC–7. Fe–MOF pattern shows typical diffraction peaks at 9.34°, 10.44°, 16.67°, 18.65°, and 20.92° corresponding to (002), (101), (103), (200), and (202) crystal planes inferring successful synthesis of Fe–MOF with good crystallinity and consistent with those reported in the literature[36,37]. The main diffraction peaks at 9.34° and 10.44° are also evident in PM–7 and PMC–7 but with reduced intensity due to the presence of Fe–MOF (7%) in the PVDF and PVP matrix.

As depicted in Fig. 1b, the Fourier transform infrared spectroscopy (FTIR) spectra of the Fe–MOF showed absorption peaks at 3474 and 3364 cm^{-1} attributed to the –NH$_2$ bonds symmetric and asymmetric vibrations, respectively. The adsorption band at 1652 cm^{-1} is associated with C=N stretching vibration. Peaks at 1575 and 1377 cm^{-1} are assigned to the asymmetric and symmetric carboxyl group vibrations, respectively[38]. Meanwhile, bands at 1253 and 765 cm^{-1} are attributed to the C–N stretching in the benzene ring and C–H bending vibrations in the organic linkers, respectively. In addition, bands at 770, 575, and 433 cm^{-1} are ascribed to the O–Fe–O and Fe–O vibration modes[39]. β–CD showed a broad peak at 3320 cm^{-1} associated with the –OH group. Moreover, peaks at 2930, 1648, and 1156 are linked to C–H, H–O–H, and C–O vibrations, respectively. Notably, the sharp peak at 1020 cm^{-1} is linked to C–O–C and C–OH stretching vibrations[40]. The peak at 938 cm^{-1} is ascribed to the skeletal vibration of α-1,4 linkages in the β–CD structure[41]. Furthermore, for PM–7 and PMC–7 membranes, the peaks observed at 1079 and 1402 cm^{-1} are associated with the C–C and C–H bonds in the PVDF matrix[42]. The absorption peak at 879 cm^{-1} is ascribed to the α-phase of the PVDF. Besides, the peaks at 612 and 487 cm^{-1} are linked to the –CF$_2$ bending vibrations[43].

Figure 1c illustrates the Raman spectra of the PMC–7 and Fe–MOF. The band at 1127 cm^{-1} is assigned to C–COO vibrations. Bands at 827, 1127, and 1620 cm^{-1} are attributed to the vibrations in the benzene ring of the MOF[44]. Bands at 1162 and 1339 cm^{-1} represent the C–H and C–O bending vibrations in the benzene ring and the –COOH group of the MOF ligand, respectively. Furthermore, bands at 1256 and 1423 cm^{-1} are attributed to the C–NH$_2$ and –COO vibrations in the MOF ligand. Bands at 1580 and 1620 cm^{-1} are assigned to the C–C/C=C bonds stretching vibrations. Bands at 458 and 590 cm^{-1} are assignable to the Fe–O vibrations[45,46]. Importantly, characteristic Fe–MOF bands are present in the Raman spectra of PMC–7, further confirming the successful incorporation of the Fe–MOF in the membrane.

The thermal stability of the synthesized Fe–MOF, bare PVDF, and PMC–7 was evaluated through thermogravimetric analysis (TGA) as exhibited in the TGA weight loss curve in Fig. 1d. Fe–MOF exhibits major weight loss at 25–330 °C, which is attributable to the vaporization of the physically and chemically bound water molecules and the organic solvents trapped in the MOF. The phase loss at 330–560 °C is attributable to the ligand decomposition and the collapse of the MOF framework. The final phase loss above 600 °C represents the formation of iron oxide and carbon composites[47,48]. Bare PVDF showed excellent thermal stability up to 400 °C with one significant loss phase (72.33%) from 450–600 °C, which is attributed to polymer degradation at those elevated temperatures. Meanwhile, PMC–7 showed four phase losses. The first weight loss (2.38%) below 200 °C is attributable to the vaporization of the physically and chemically confined water molecules in the β–CD cavity and Fe–MOF. Moreover, the second minor phase (3.66%), between 200 and 385 °C, is attributable to the organic solvent removal and pyrolysis of the β–CD monomer[49]. The third stage (13.49%) is attributed to the degradation of the Fe–MOF organic
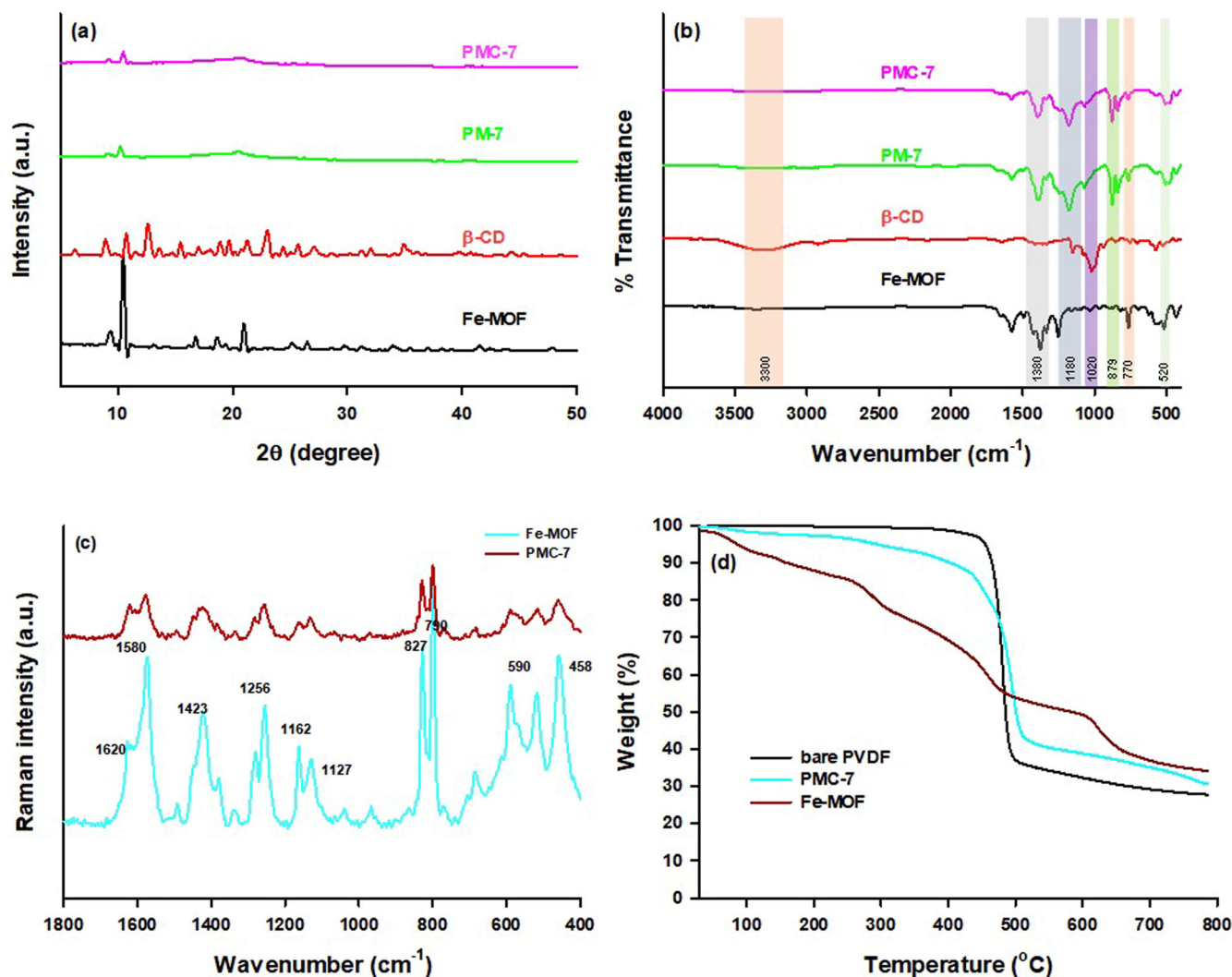
Fig. 1 | XRD, FTIR, Raman, and TGA analysis. a XRD pattern and **b** FTIR spectra of the as-prepared Fe–MOF, β–CD, PM–7, and PMC–7, and **c** Raman spectra of as-prepared PMC–7 and Fe–MOF, and **d** TGA analysis of as-prepared Fe–MOF, bare PVDF, and PMC–7.

linkers and the collapse of the skeletal structure. The final major phase loss (49.81%) above 500 °C is attributable to the polymer decomposition. Overall, PMC–7 showed a slightly higher thermal stability compared to bare PVDF membrane attributed to the addition of Fe–MOF in the PVDF membrane.

The surface morphologies of the synthesized samples were scanned using field electron scanning electron microscopy (FE-SEM) and high-resolution transmission electron microscopy (HR-TEM). As illustrated in Fig. 2a the bare PVDF shows a smooth surface with microporous structures well distributed evenly on the top surface, attributed to the phase inversion process and the inclusion of porogen (PVP). Figure 2b shows spindle-shaped crystals, which are typical of Fe–MOF. The top surface morphology (Fig. 2c) of the PMC–7 shows a smooth microporous surface with the spindle crystals distributed on the surface. Furthermore, the cross-sectional morphology (Fig. 2d) further confirms the voids in the membrane structure and the inclusion of Fe–MOF into the PVDF matrix. Figure 2e, f displays the TEM images of the as-prepared PMC–7 showing aggregated layered sheets. HR-TEM image of PMC–7 is displayed in Fig. 2g. Moreover, as illustrated in Fig. 2h shows the energy dispersive X-ray spectroscopy (EDX) spectra and the matching elemental mapping of the PMC–7, confirming the uniform dispersion C, N, O, and Fe elements and the successful synthesis of the MMM.

The elemental composition and chemical state of PMC–7 were investigated through X-ray spectroscopy (XPS). Supplementary Fig. 1

illustrates the wide XPS spectrum of the prepared PMC–7 membrane, confirming the presence of Fe, C, N, O, and F elements. Figure 3a depicts the C 1s spectra deconvoluted into different species at 284.4, 285.8, 287.2, and 290.3 eV corresponding to the C–C/C=C, C–H, and the carbon in the carboxylate (O–C=O) group in the Fe–MOF, respectively. Besides, the peaks at 285.1 eV (C–C) and 286.8 eV (C–N/C–F) are associated with the –CF_2 in the PVDF and alkyl group in the benzene ring of the Fe–MOF[50,51]. Moreover, the high-resolution O 1s spectra profile (Fig. 3b) was deconvoluted into three peaks at 531.4, 531.6, and 532.5 eV, corresponding to the Fe–O, C=O, and the O–C=O, respectively[52]. Furthermore, Fig. 3c illustrates the Fe 2p spectrum, which shows a characteristic peak at 711.8 and 724.4 eV corresponding to the Fe $2p_{3/2}$ and Fe $2p_{1/2}$ of Fe–MOF, respectively[53]. In addition, peaks at 707.1, 716.9, and 734.6 eV confirm the presence of Fe^{3+} oxidation states in the as-prepared PMC–7 membrane[54]. Meanwhile, Fig. 3d exhibits the F 1s spectrum showing a characteristic peak at 685.6 eV belonging to the C–F bond in the PVDF matrix[55].

The membrane's hydrophilicity/hydrophobicity was determined through static water contact angle (WCA) measurements. As displayed in Fig. 4a, the bare PVDF had an average water contact angle of ~67.90° indicating good hydrophilicity. The inclusion of Fe–MOF in the PVDF matrix (Fig. 4b) slightly increased the hydrophilicity of the PM–7 membrane (~66.55°). The β–CD surface functionalization further reduced the
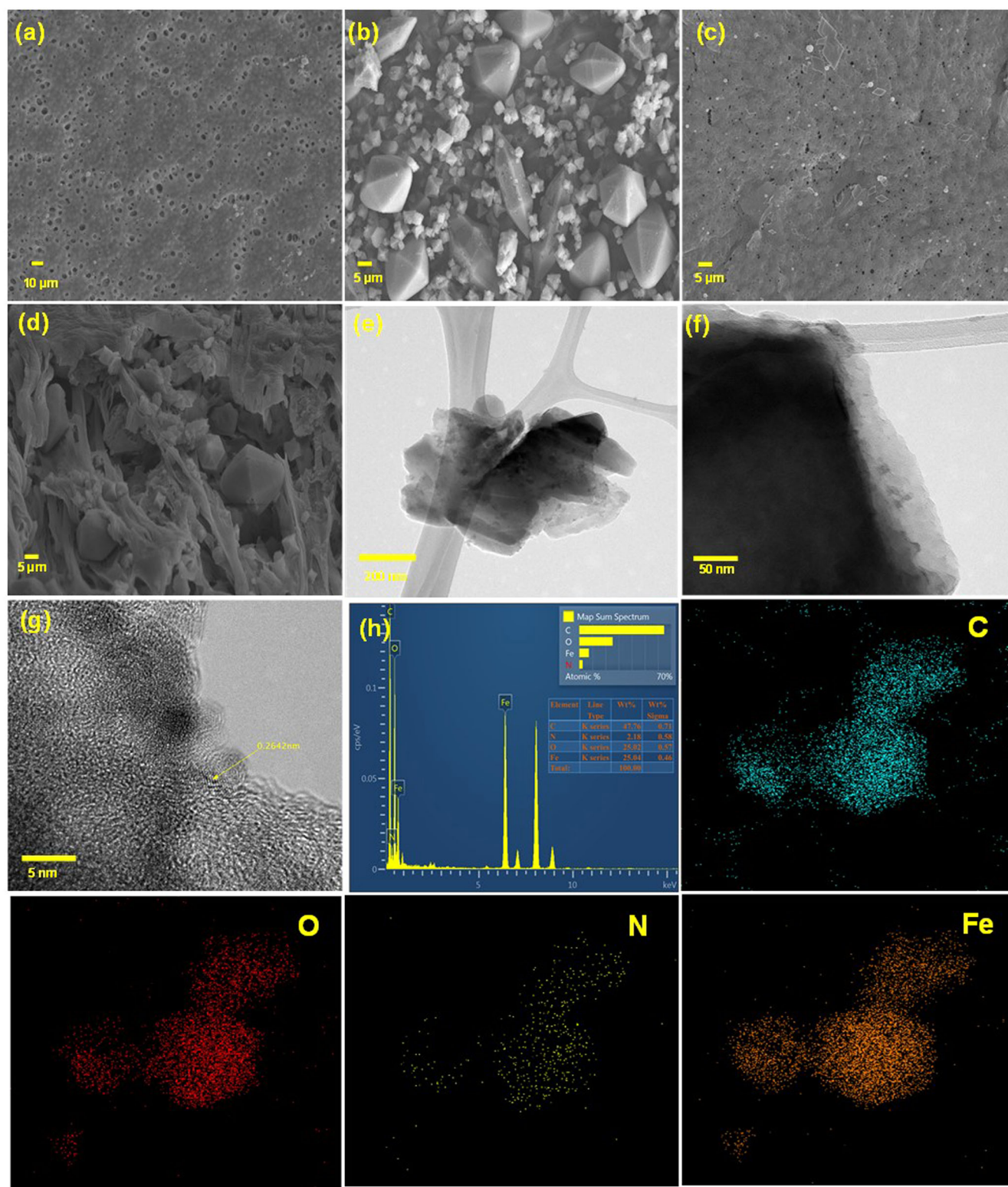
Fig. 2 | Morphological analysis. FE-SEM images of **a** bare PVDF membrane, **b** Fe–MOF, **c** top surface morphology, **d** cross-section morphology, **e, f** TEM images, **g** HR-TEM image, and **h** EDX spectra and corresponding elemental mapping of PMC–7.

contact angle (~55.65°), making the PMC–7 membrane more hydrophilic, which is ideal for a membrane adsorbent in aqueous solutions. Importantly, PVP, commonly used as a polymer additive to alter the membrane porosity, is hydrophilic in nature and could have improved the hydrophilicity of the membrane[56]. Besides, the enhanced hydrophilicity of the PMC–7 can be

attributed to the plentiful –OH groups in the hydrophilic external surfaces of the β–CD.

The nitrogen adsorption–desorption isotherm of Fe–MOF is illustrated in Supplementary Fig. 2. The MOF exhibited a typical type IV isotherm with an H3 hysteresis loop. The Fe–MOF had a
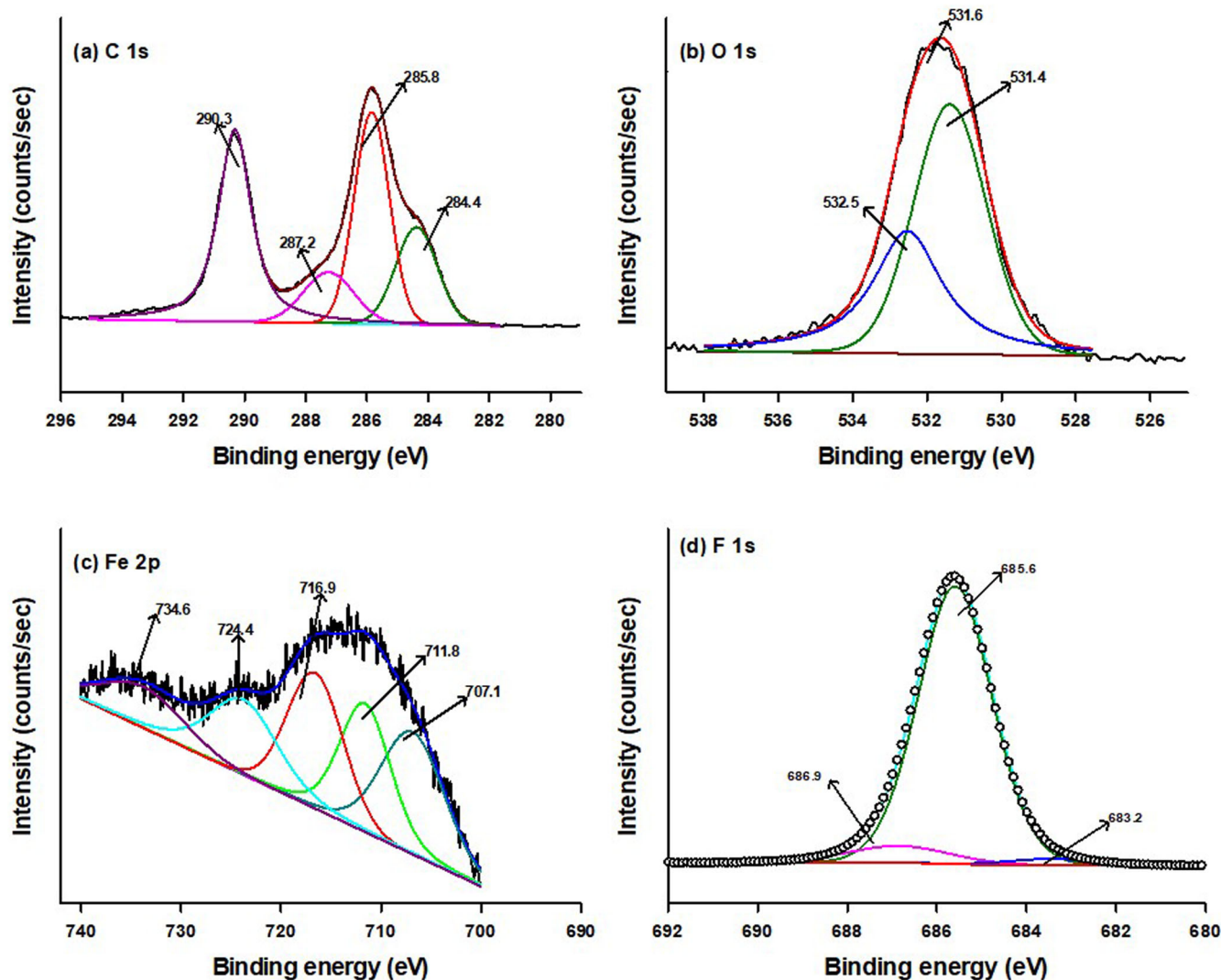
Fig. 3 | XPS analysis. High-resolution **a** C 1*s*, **b** O 1*s*, **c** Fe 2*p*, and **d** F 1*s* XPS spectra of PMC–7.
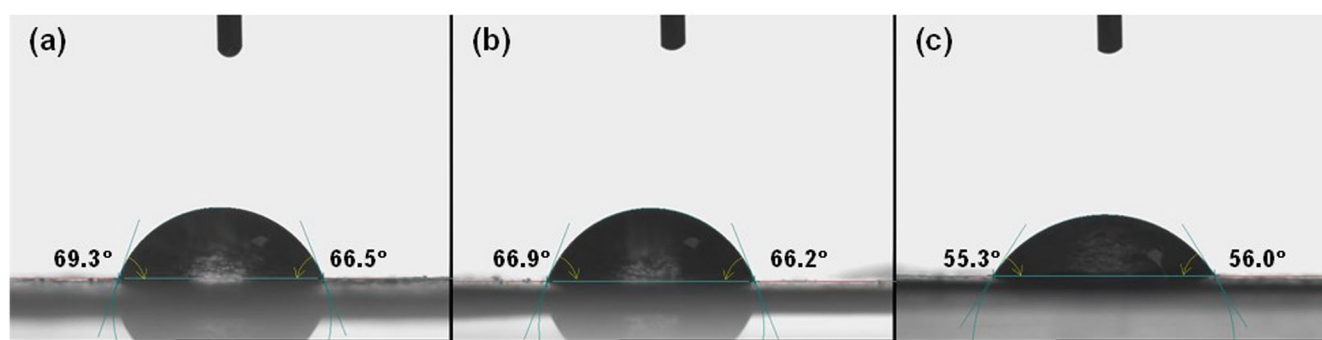

Fig. 4 | Contact angle analysis. Static water contact angle of **a** bare PVDF, **b** PM–7, and **c** PMC–7.

Brunauer–Emmett–Teller (BET) SSA, average pore diameter, and total pore volume of $682.4\,m^2\,g^{-1}$, 2.534 nm, and $0.432\,cm^3\,g^{-1}$, respectively. The mesoporous architecture is key in providing active sites for pollutant adsorption. Moreover, porosity and pore size distribution were evaluated and illustrated in Fig. 5 using an automatic mercury intrusion porosimeter, and the results are summarized in Table 1. The bare PVDF, PMC–3, PMC–7 without PVP, PMC–7, PMC–3, and PMC–10 membranes had an average

pore diameter of 882.5, 452.2, 196.0, 395.0, and 324.1 nm, respectively. To further elucidate the synergistic effect of PVP on the membrane performance, porosity and adsorption experiments were performed. The porosity of the bare PVDF, PMC–3, PMC– 7 without PVP, PMC–7, and PMC–10 was 83.19, 82.28, 65.23, 77.70, and 63.11%, respectively. Thus, the inclusion of PVP in the casting solution significantly enhanced the MMM porosity as displayed in Fig. 5b. PVP hydrophilicity promotes the formation of macro
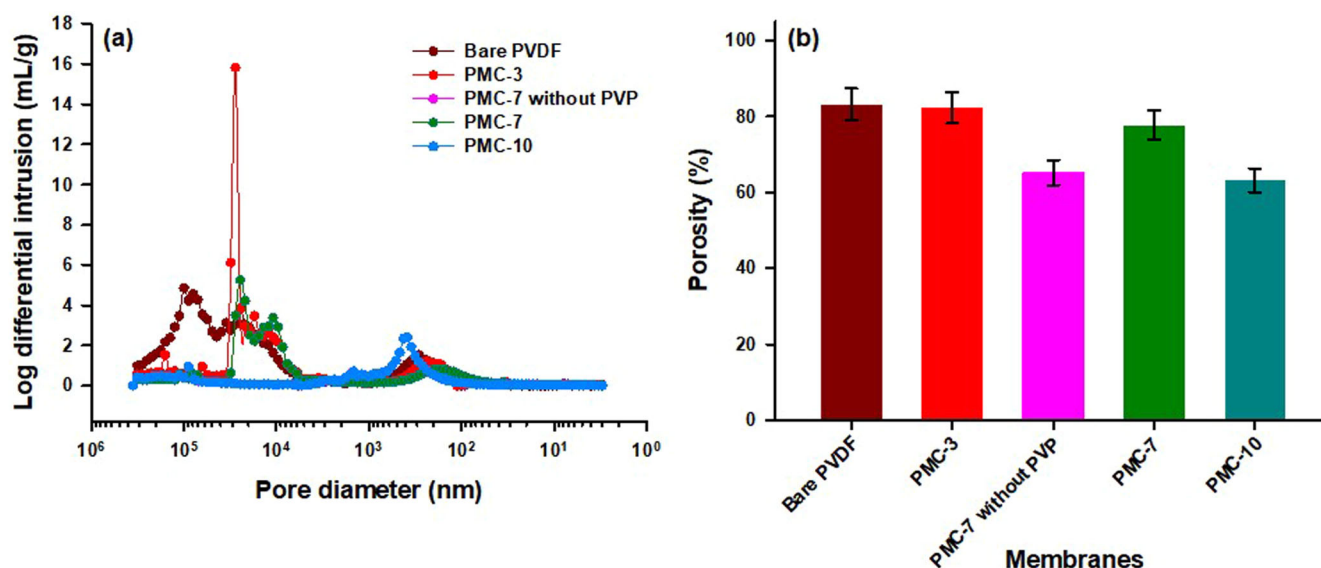
Fig. 5 | Pore structure analysis. a Pore size distribution and **b** porosity of bare PVDF, PMC–3, PMC–7 without PVP, PMC–7, and PMC–10.

Table 1 | Pore structure characterization

Membrane	Porosity (%)	Total pore area ($m^2 g^{-1}$)	Total intrusion volume ($mL g^{-1}$)	Average pore diameter (nm)	Bulk density ($g mL^{-1}$)	Apparent density ($g mL^{-1}$)
Bare PVDF	83.19	23.92	5.278	882.5	0.158	0.938
PMC–3	82.28	36.70	4.149	452.2	0.198	1.119
PMC–7 without PVP	65.23	32.83	1.609	196.0	0.406	1.166
PMC–7	77.70	30.06	2.969	395.0	0.262	1.174
PMC–10	63.11	29.82	2.417	324.1	0.261	0.708

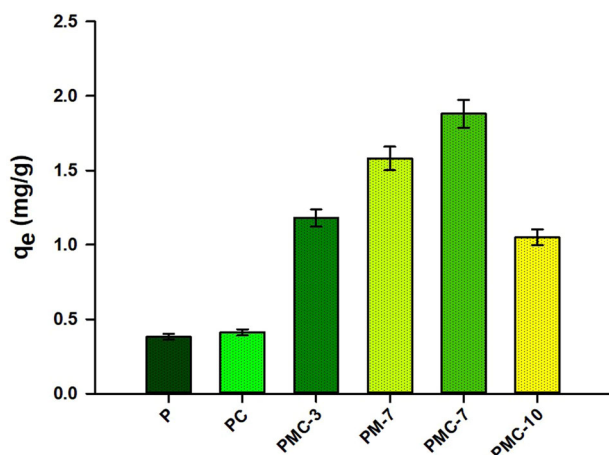Porosity and pore size distribution of bare PVDF, PMC–3, PMC–7 without PVP, PMC–7, and PMC–10.

Fig. 6 | Adsorption performance. Adsorption capacity of CIP over P, PC, PMC–3, PM–7, PMC–7, and PMC–10 (Experimental conditions: $[CIP]_0 = 10 mg L^{-1}$, adsorption time = 360 min, pH = 6, and temperature = 25 ± 2 °C). The error bars represent the mean ± standard deviation.

voids in the PVDF membrane during the phase inversion process as well as the mechanical strength of the fabricated membrane[57,58]. Notably, as presented in Supplementary Table 1, the performance of the PMC–7 with PVP was superior in contrast to PMC–7 without PVP, with removal efficiencies of 87.6 and 54.4%, respectively.

Adsorption performance

Figure 6 illustrates the comparison of the different fabricated membranes for the adsorption of CIP. PMC–7 showed the best removal performance with 1.9 mg g^{-1}, which is fivefold the performance of bare PVDF. The performance improved with an increase in the MOF ratio, with 7% being the most optimal ratio. It's worth noting that a further increase resulted in a decline in the removal performance, as shown in PMC–10, which can be ascribed to blockage of the pores and active sites inside the polymer matrix as confirmed by a decrease in the porosity of PMC–10. PM-7 and PMC–7 were chosen for the subsequent adsorption experiments.

As demonstrated in Fig. 7, the influence of contact time on adsorption capacity and removal efficiency was investigated. The adsorption occurred rapidly in the first 60 min, and then the rate gradually decreased until adsorption equilibrium was established as the active sites diminished. Notably, the highest adsorption capacity and the removal rate for PMC–7 were 1.9 mg g^{-1} and 87.6%, respectively compared to 1.6 mg g^{-1} and 78.9% for PM–7. The adsorption in PM–7 can be associated with the considerable SSA and the porous nature of the Fe–MOF, which provide accessible and abundant adsorption sites. Besides, enhanced adsorption performance could be attributed to the β–CD functionalization on the surface of PMC–7 through different interaction mechanisms[59,60]. Meanwhile, the adsorption kinetic curves were fitted to the three adsorption kinetic models, namely pseudo-first-order (PFO), pseudo-second-order (PSO), and Elovich models, as depicted in Fig. 7a. Supplementary Information provides a detailed discussion of the adsorption kinetics. The corresponding rate constants and correlation coefficient (R^2) values are summarized in Supplementary Table 2. Comparatively, for PM–7 and PMC–7, the PSO model corresponded most closely to the experimental results, with higher R^2 (0.999) and lower χ^2 values, thus suggesting a chemisorption process for the adsorption of CIP onto PMC–7.
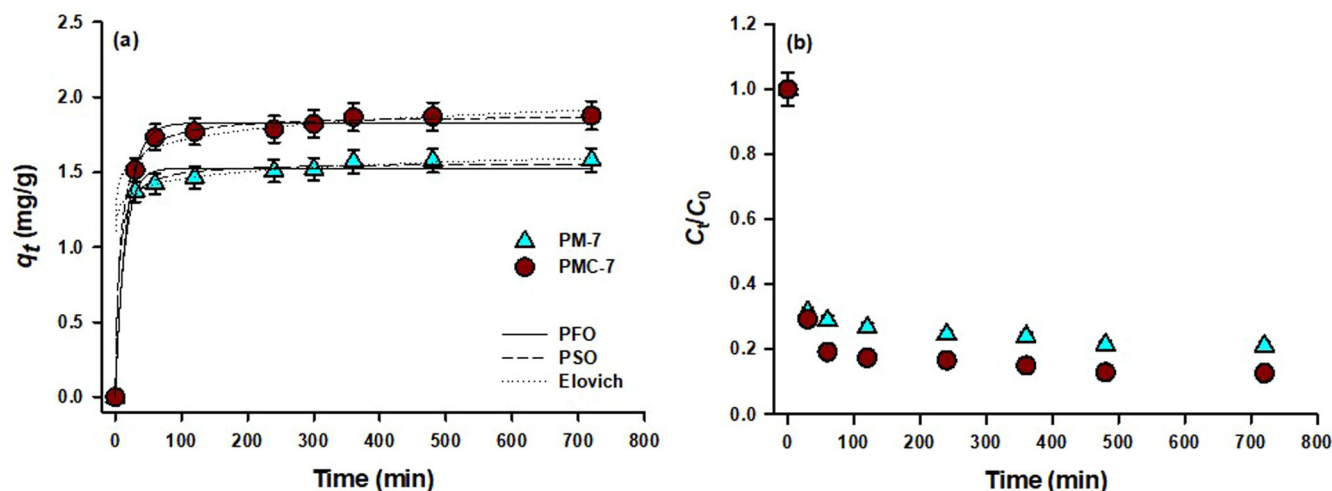
Fig. 7 | Adsorption kinetics. Effect of contact time on adsorption capacity and removal rate for CIP over PM–7 and PMC–7 (Experimental conditions: $[CIP]_0 = 10$ mg L^{-1}, adsorption time = 0–720 min, pH = 6, and temperature = 25 ± 2 °C). The error bars represent the mean ± standard deviation.
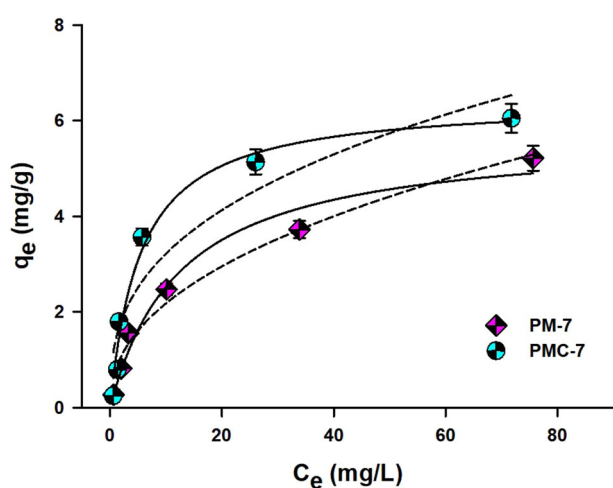

Fig. 8 | Adsorption isotherms. Effect of CIP concentration on adsorption capacity over PM-7 and PMC-7. Solid and dashed lines indicated curves fitted using the Langmuir and Freundlich isotherm models (Experimental conditions: $[CIP]_0 = 1–100$ mg L^{-1}, adsorption time = 360 min, pH = 6, and temperature = 25 ± 2 °C). The error bars represent the mean ± standard deviation.

To better elucidate the adsorption behavior of PM–7 and PMC–7 membranes, adsorption isotherm experiments were performed as depicted in Fig. 8. Langmuir and Freundlich isotherm models were employed to fit the obtained experimental data. The corresponding fitting parameters, R^2, and the χ^2 values are summarized in Supplementary Table 3. For PM–7 and PMC–7, the PSO model best fitted the experimental results based on the higher R^2 and lower χ^2 values. Importantly, the Langmuir and Freundlich isotherm models R^2 values for PMC–7 were 0.981 and 0.898, respectively, suggesting that the CIP adsorption was a homogeneous monolayer process. Besides, the dimensionless factor (R_L) values ranged between 0 and 1, suggesting that the adsorption process was favorable. Moreover, the maximum adsorption capacity (q_m) was 6.43 mg g^{-1}. A comparison of the adsorption capacities of previously reported adsorbents is presented in Supplementary Table 4.

Effect of pH
Solution pH is a key variable that influences the adsorption process by altering the adsorbent surface charge, degree of ionization, and CIP speciation. CIP ($pK_{a,1} = 6.09$ and $pK_{a,2} = 8.74$) can exist as cationic CIP$^+$ (pH < 6.09), zwitterionic CIP$^\pm$ (pH = 6.09–8.74), and anionic, CIP$^-$ (pH > 8.74)[61]. To gain further insight into the effect of pH on the removal of CIP onto PMC–7, the adsorption performance was evaluated at different pHs (3–11) as exhibited in Supplementary Fig. 3a. Furthermore, as displayed in Supplementary Fig. 3b the zeta potential of PMC–7 was negatively charged for all pH values, and the surface charge decreased with an increase in pH. The removal rates at pH 3, 5, 7, 9, and 11 were 76.0, 82.5, 86.7, 81.9, and 64.3%, respectively, suggesting that the adsorption was more favorable at pH 7. The adsorption performance between pH 3–7 can be attributed to electrostatic interactions between the cationic CIP$^+$ and zwitterionic CIP$^\pm$ forms and the negatively charged membrane. On the other hand, in alkaline conditions, the decrease in performance at pH 9 and 11 can be attributable to electrostatic repulsion that exists between the anionic CIP$^-$ and the negatively charged membrane at high pH values. This suggests the involvement of other mechanisms in the adsorption of the pollutant.

Effect of coexisting ions and reusability
The presence of various anions and cations in aqueous solutions may affect the removal of organic pollutants. The effect of coexisting anions such as chloride (Cl$^-$), bicarbonate (HCO$_3^-$), sulfate (SO$_4^{2-}$), and nitrate (NO$_3^-$) for the removal of CIP was illustrated in Supplementary Fig. 4. The order of interference was as follows Cl$^-$ > SO$_4^{2-}$ > NO$_3^-$ > HCO$_3^-$. Cl$^-$ caused the most inhibitory effect to have 75.6% removal efficiency, followed by SO$_4^{2-}$, which resulted in a 77.9% removal efficiency, NO$_3^-$ resulted in an 84.9% removal efficiency, and finally, HCO$_3^-$, which exhibited minimal interference on CIP adsorption with an 86.9% removal efficiency. The reduction could be attributed to the competition with the CIP moieties for the active sites on the MMM surface[62]. Moreover, the effect of cations (Pb^{2+}, K$^+$, Zn^{2+}, and Mg^{2+}) on the removal of CIP was investigated, as depicted in Supplementary Fig. 4. The order of interference was as follows: Zn^{2+} > Pb^{2+} > Mg^{2+} > K$^+$, with 78.6, 81.2, 82.0 and 82.3% removal efficiencies, respectively. The inhibitory effect on the removal performance in the presence of coexisting ions is attributed to the competition for plentiful active sites through electrostatic interactions and complexation effects between the cations and the negatively charged PMC–7[63]. Furthermore, to investigate the feasibility of practical applications of the synthesized PMC–7 a comparative analysis was performed using different water sources such as tap water (from our laboratory), surface water (Sincheon river water, Daegu), and wastewater (Sincheon sewage treatment plant, Daegu). As illustrated in Supplementary Fig. 5, the observed removal efficiencies slightly reduced in the tap water (86.8%), surface water (83.2%), and wastewater (81.6%), and this can be attributed to the various coexisting ions in the water, which might interfere with the adsorption process. The efficient removal efficiencies in different
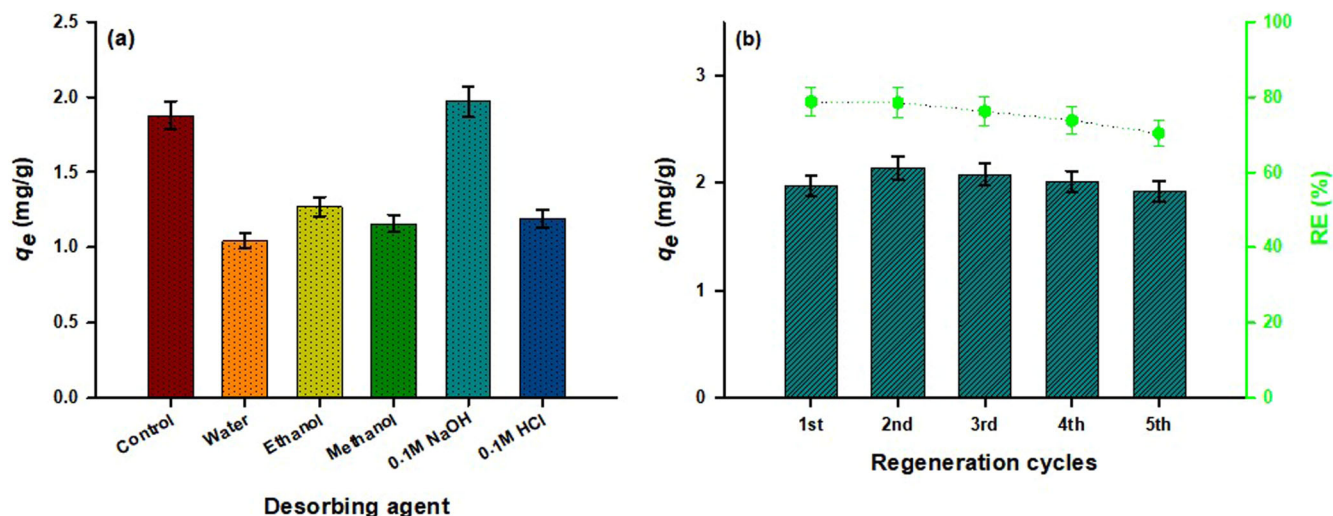
Fig. 9 | Reusability of PMC–7. a Effect of different desorbing agents on the adsorption of CIP over PMC–7. **b** Five regeneration cycles for CIP adsorption over PMC–7 using 0.1 M NaOH as a desorbing agent (Experimental conditions: $[CIP]_0 = 10$ mg L^{-1}, adsorption time = 360 min, and temperature = 25 ± 2 °C). The error bars represent the mean ± standard deviation.
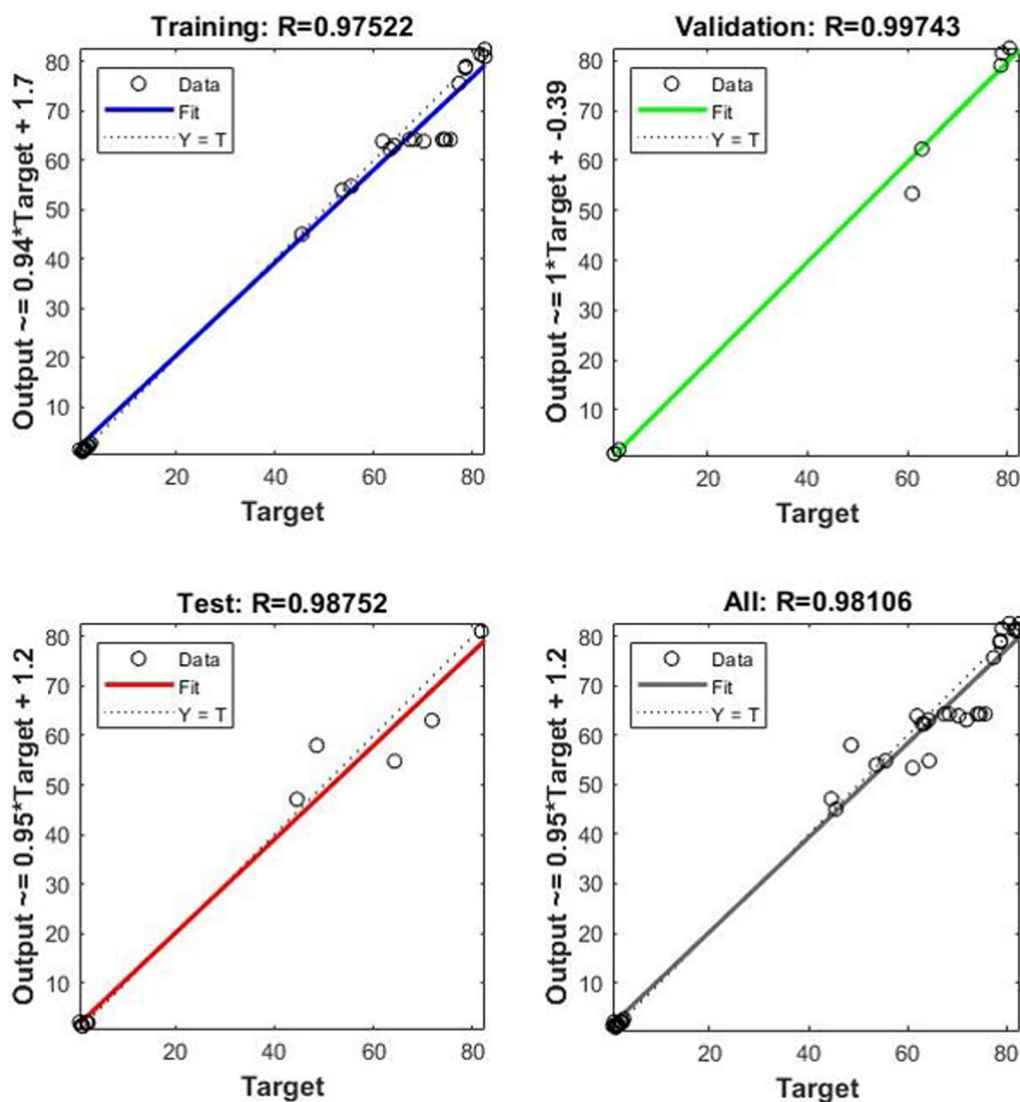

Fig. 10 | Prediction of adsorption efficiency. Training, validation, testing, and all dataset plots for the evaluation of the ANN model in the removal of CIP.
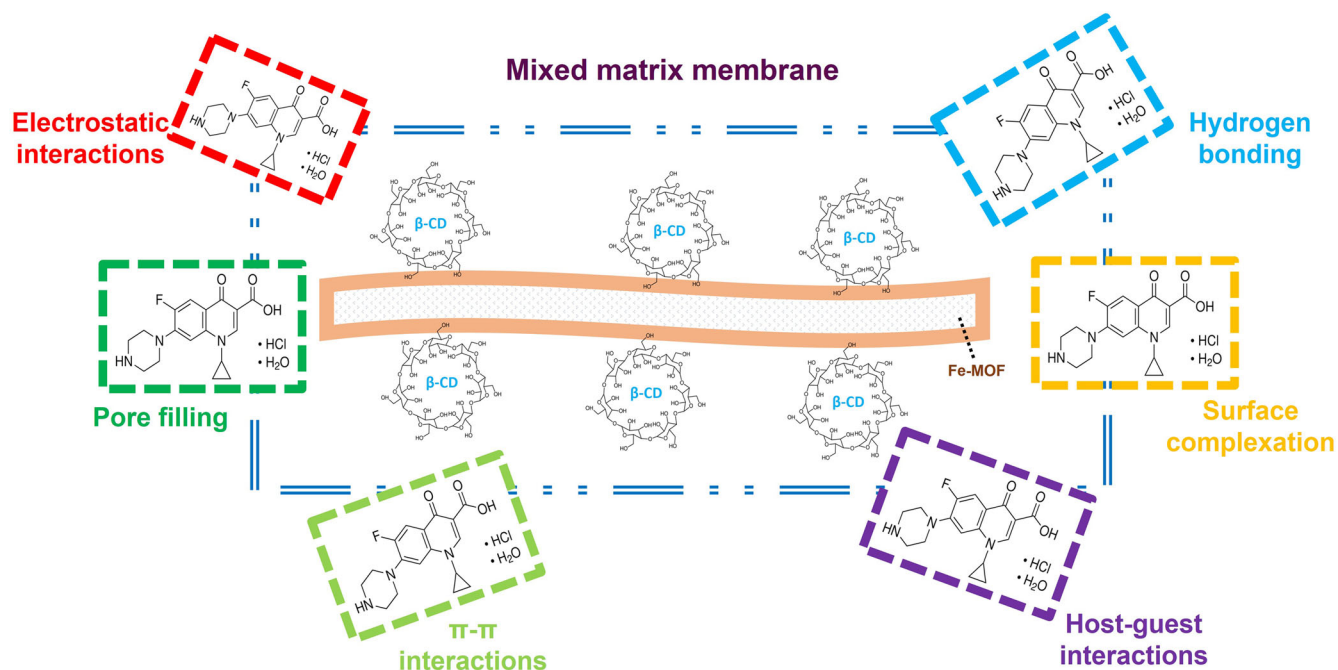
Fig. 11 | Mechanism of study. Proposed adsorption mechanism for the removal of CIP over PMC–7.

water sources indicate that PMC–7 has an exciting prospect to be used in the practical applications for the removal of CIP.

The reusability of the optimized PMC–7 was evaluated using different desorbing agents, including water, ethanol, methanol, 0.1 M NaOH, and 0.1 M HCl, as depicted in Fig. 9a. 0.1 M NaOH showed the best performance after one cycle and was therefore used in five subsequent cycles as depicted in Fig. 9b. It's worth noting that the spent membrane after each cycle was washed in the desorbing agent, rinsed with DI water, and left to dry in ambient conditions before the next cycle. The adsorption performance gradually decreased with each cycle, attributed to the loss of materials and several active sites in the membrane. Notably, the hydrophilic and macroporous membrane showed good reusability with over 70% removal efficiency after five successive adsorption–desorption cycles. The XRD profile before and after the adsorption (Supplementary Fig. 6) shows a decrease in the intensity of the peak, which can be attributed to the adsorption of CIP onto PMC–7. However, the main diffraction peaks are evident in the used PMC–7, suggesting that the membrane maintained its structural integrity and thus good mechanical stability. In addition, the iron leaching concentrations (Supplementary Table 5) for Fe–MOF and PMC–7 are below the required discharge standards. The great reusability and easy separation suggest that the PMC–7 is a potential adsorbent for the removal of CIP in large-scale operations. However, real-life and industrial applications are more difficult because of complex pollutants and coexisting ions composition, and therefore future studies should be conducted to investigate the removal of various contaminants using the MMM adsorbent as well as scale-up studies to measure the viability of an industrial application. Moreover, column adsorption studies should be conducted for the removal of various organic pollutants.

Artificial neural network
The artificial neural network (ANN) was employed to predict the adsorption efficiency for CIP. A multilayered feed-forward network comprising of input, hidden, and output (neurons) layers employed the Levenberg-Marquardt backpropagation learning algorithm[30]. The ANN model had four input variables (time, pH, temperature, and mass) and two output variables (adsorption capacity and removal efficiency). Furthermore, the number of hidden neurons was chosen as 10, as shown in the topology of the developed ANN network (Supplementary Fig. 7). A random set of

experiments was developed using the Design-Expert software. The ANN modeling and calculations were performed using MATLAB 2021a neural network toolbox. The obtained datasets were randomly selected for training (70%), validation (15%), and testing (15%) of the ANN model. Moreover, the regression (R) and mean square error (MSE) values were employed as the performance metric as described in Supplementary Information. The R values for training, validation, testing, and overall were 0.975, 0.997, 0.988, and 0.981, respectively, as illustrated in Fig. 10. The high R values imply the closeness of the obtained and predicted value and further underscores the potential of ANN in the prediction of the removal of CIP. Performance, training state, and error histogram plots are illustrated in Supplementary Fig. 8.

Proposed adsorption mechanism
The FTIR patterns before and after adsorption (Supplementary Fig. 9) showed a shift and change in the intensities in some peaks, suggesting the involvement of various functional groups in the CIP adsorption. The significant reduction in the peak around 3320 cm^{-1} suggests the interaction of the –OH and –NH$_2$ bonds with CIP. Besides, the peak corresponding to the C–H bond at 2916 cm^{-1} had a considerable decrease in intensity after the CIP adsorption. Similarly, the peak at 1020 cm^{-1} reduced intensity and was shifted to 1075 cm^{-1}, suggesting the involvement of the C–O–C groups. The peak corresponding to the C=N stretching vibrations at 1652 cm^{-1} increased in intensity and was shifted to 1575 cm^{-1}. In addition, a new peak appeared at 1388 cm^{-1}, suggesting the interactions of the carboxyl groups and CIP. Moreover, as depicted in Supplementary Fig. 10, the analysis of the XPS profiles before and after the adsorption of CIP was assessed and compared to gain insights into the involvement of various functional groups and bonds in the adsorption of the target pollutant. The C 1s spectra profiles (Supplementary Fig. 10a) showed a peak shift in the binding energies, confirming the involvement of C–C/C–H, C–C/C=C, and O–C=O in the adsorption via π–π interactions and hydrogen bonding. The O 1s XPS profiles (Supplementary Fig. 10b) illustrate a shift of the binding energies inferring a strong interaction existed between CIP (–OH and –NH$_2$) and O/N containing functional groups via electrostatic interactions and hydrogen bonding[64]. This is confirmed by the plentiful hydrogen donors and acceptors in the CIP molecule and the synthesized MMM. Moreover, Fe 2p XPS spectra (Supplementary Fig. 10c) showed a shift in the binding energies and
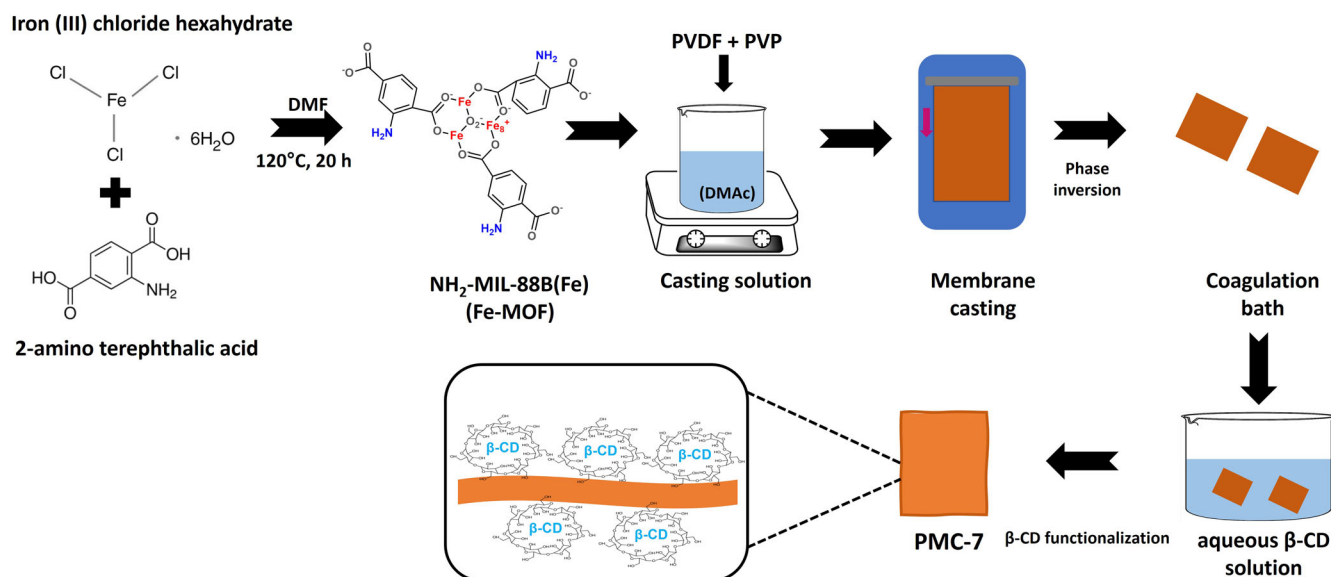
Fig. 12 | Synthesis of materials. Schematic illustration of the preparation of the mixed matrix membranes.

a slight increase in the intensity of the peaks, proving an interaction between Fe-containing groups and CIP. Moreover, the Fe–O group can interact with the CIP molecule via the metal surface complexation mechanisms[65,66].

Notably, the high porosity confirmed by the mercury intrusion porosimeter and the high surface areas of the Fe–MOF, and PMC–7 can provide accessible active sites for the binding of the CIP. This suggests the pore filling/adsorption mechanism is plausible for the adsorption of CIP into the macroporous membrane as described in the literature[67,68]. The aromatic ring moieties in the target pollutant can interact with the benzene rings in the PMC–7 structure via the π–π electron donor–acceptor interactions, thereby facilitating more adsorption[69]. Besides, β–CD (host molecule) can form inclusion complexes with CIP (guest molecule) in the hydrophobic cavity aided by forces such as van der Waals interactions and hydrogen bonding[59,70]. As discussed in the effect of pH, the electrostatic interactions exist between the negatively charged PMC–7 and the cationic CIP^+ and zwitterionic $CIP^{\pm}$ forms, further promoting the adsorption process. The adsorption mechanism for the removal of CIP onto PMC–7 is summarized in Fig. 11.

Overall, we present a facile technique for the construction of a β–CD surface functionalized PVDF–MOF mixed matrix membrane for the enhanced adsorptive removal of CIP. A porous and hydrophilic PMC–7 membrane fabricated through the phase inversion technique exhibited excellent performance with 87.6% removal efficiency and the maximum adsorption capacity was 6.43 mg g^{-1}. The inclusion of hydrophilic pore-forming additive, PVP, in the casting solution significantly enhanced the MMM porosity as well as the hydrophilicity, which is critical in providing active sites for antibiotic removal. Furthermore, the improved hydrophilicity of the PMC–7 can be attributed to β–CD surface modifications due to the plentiful –OH groups in the hydrophilic external surfaces of the β–CD. Significantly, the synthesized macroporous membrane showed good reusability with over 70% removal efficiency after five successive adsorption–desorption cycles. The plausible adsorption mechanism can be attributed to the synergistic involvement of electrostatic interactions, surface complexation, hydrogen bonding, π–π interactions, and host-guest inclusion mechanisms. The findings and insights from this study suggest that the PMC–7 membrane had great potential for the removal of CIP and shows promise for MMM in the adsorption of various organic pollutants.

Methods
Materials
Polyvinylidene fluoride powder (PVDF, M.W.: 543,000), β-cyclodextrin (β–CD, ≥97.0%) 2-amino terephthalic acid (NH$_2$BDC, 99.0%), N,N-dimethyl formamide (DMF, 99.5%), N,N-dimethylacetamide (DMAc, 99.0%), sodium hydroxide (NaOH, 98%), ferric chloride hexahydrate (FeCl$_3$·6H$_2$O, >98.0%), hydrochloric acid (HCl, 99.8%), methanol (CH$_3$OH, 99.8%), and ethanol (C$_2$H$_5$OH, 99.5%) were acquired from Sigma Aldrich (St. Louis, MO, USA). Acetonitrile (CH$_3$CN, 99.8%) and ciprofloxacin hydrochloride monohydrate (C$_{17}$H$_{18}$FN$_3$O$_3$·HCl·H$_2$O, lyophilized powder) were obtained from Fisher Scientific. Formic acid (CH$_2$O$_2$, >85%), and polyvinylpyrrolidone (PVP) were purchased from Dae-Jung Chemicals (Siheung, Gyeonggi, Republic of Korea). All the chemicals and reagents were used directly without further pretreatment. Supplementary information provides detailed characterization methods for the materials and as-prepared samples. The physicochemical properties of CIP and β–CD are provided in Supplementary Tables 6, 7, respectively.

Synthesis of Fe–MOF
The solvothermal technique was used to synthesize Fe–MOF, as described in the literature with little modifications[54]. Typically, 2.51 g amino terephthalic acid and 3.74 g FeCl$_3$ · 6H$_2$O were dissolved in 300 mL of DMF solution and stirred for 2 h and afterward sonicated for 0.5 h at room temperature. The aforementioned solution was placed in a Teflon-lined autoclave, heated to 120 °C, maintained for 20 h, and then cooled to room temperature. The solution was centrifuged, and the resultant powder was rinsed with DMF and washed with EtOH three times. Subsequently, the Fe–MOF was dried at 80 °C for 12 h and was further utilized to prepare the mixed matrix membranes.

Preparation of mixed matrix membrane
Typically, a predetermined amount of Fe–MOF was dispersed in DMAc solvent under sonication for 0.5 h. Then, PVDF and PVP powders were poured into the solution and magnetically stirred at 60 °C for 12 h to form a homogenous casting solution. The casting solution was left to cool under ambient conditions to remove the bubbles and then spread on the glass plate using a bar coater with a thickness of 100 μm. The membranes were immersed in a distilled water coagulation bath at room temperature for 24 h for the phase inversion process. The as-prepared PVDF-MOF membranes were immersed in a β–CD aqueous solution for 24 h for surface functionalization and subsequently washed with de-ionized water and dried in ambient conditions and denoted as PMC. Bare PVDF, PVDF without MOF, and PVDF without β–CD functionalization membranes were also prepared using the same procedure and denoted as P, PC, and PM, respectively. Meanwhile, membranes with varying MOF weight ratios (3, 7, and 10%)

were prepared and labeled as PMC–3, PMC–7, and PMC–10, respectively. The casting solution composition of the prepared membranes is presented in Supplementary Table 8. The preparation route is shown in Fig. 12.

Experimental protocol

Ciprofloxacin hydrochloride monohydrate (CIP) was dispersed in nano-pure water to form a stock solution with an initial concentration of 10 mg L^{-1}. A blank test was performed without the adsorbent added to the solutions to assess any interferences between the wall of poly-ethylene (PE) bottles and the filter apparatus. Batch adsorption experiments were performed under ambient conditions, to determine the adsorption behavior of the as-prepared mixed matrix membranes (MMMs). The adsorption experiments were performed by adding MMMs, with predetermined weight, in the 50 mL PE bottles con-taining 30 mL of the CIP solutions and shaking at 150 rpm for 12 h. The solution pH values were adjusted with 0.1 M HCl and/or 0.1 M KOH. After the adsorption, the thin MMMs were removed, and the residual concentrations in the supernatant were analyzed.

To measure the concentration of the target pollutant, high-performance liquid chromatography (HPLC, Waters Technologies, Waters Alliance 2695 series, USA) coupled to a photodiode array system (PDA 2996 detector, Waters) was used to analyze the concentration of CIP. The chromatographic measurement of the CIP was performed at a wave-length of 272 nm by using the Intersil ODS-3 100 Å column (150 × 4.6 mm, 5 μm particle size, GL Science, Japan), and the temperature was maintained at 40 ℃. About 10 μL of sample volume was injected during the analysis, and a mixed solution of methanol and 0.1% of formic acid with a volume ratio of 30:70 (v v^{-1}) was used as a mobile phase at a flow rate of 1 mL min^{-1}. The equilibrium adsorption capacity (q_e) and the removal efficiency (RE) were calculated from Eqs. 1 and 2, respectively:

$$\text{Adsorption capacity}, q_e \left(\text{mg g}^{-1}\right) = \frac{C_o - C_e}{m} V \qquad (1)$$

$$\text{Removal efficiency}, \text{RE}(\%) = \left(\frac{C_o - C_e}{C_o}\right) \times 100 \qquad (2)$$

where q_e is the amount of concentration of CIP adsorbed on the adsorbent (mg g^{-1}); C_0 and C_e are the initial and equilibrium concentration (mg L^{-1}), respectively; V is the volume of the solution (L); and m is the mass of adsorbent (g). All the experiments were performed in triplicates.

Data availability

The data that support the findings of this study are available from the corresponding author upon reasonable request.

References

1. Tatarchuk, T., Soltys, L. & Macyk, W. Magnetic adsorbents for removal of pharmaceuticals: a review of adsorption properties. *J. Mol. Liq.* **384**, 122174 (2023).
2. Sodhi, K. K. & Singh, D. K. Insight into the fluoroquinolone resistance, sources, ecotoxicity, and degradation with special emphasis on ciprofloxacin. *J. Water Process Eng.* **43**, 102218 (2021).
3. Igwegbe, C. A., Oba, S. N., Aniagor, C. O., Adeniyi, A. G. & Ighalo, J. O. Adsorption of ciprofloxacin from water: A comprehensive review. *J. Ind. Eng. Chem.* **93**, 57–77 (2021).
4. Ganthavee, V. & Trzcinski, A. P. Removal of pharmaceutically active compounds from wastewater using adsorption coupled with electrochemical oxidation technology: a critical review. *J. Ind. Eng. Chem.* **126**, 20–35 (2023).
5. Masud, M. A. A., Annamalai, S. & Shin, W. S. Remediation of ciprofloxacin in soil using peroxymonosulfate activated by ball-milled

6. Khanzada, N. K. et al. Removal of organic micropollutants using advanced membrane-based water and wastewater treatment: a review. *J. Membr. Sci.* **598**, 117672 (2020).
7. Mahmoudi, F. et al. Application of perovskite oxides and their composites for degrading organic pollutants from wastewater using advanced oxidation processes: review of the recent progress. *J. Hazard. Mater.* **436**, 129074 (2022).
8. Pan, Y. et al. Facile construction of Z-scheme Fe-MOF@BiOBr/M −CN heterojunction for efficient degradation of ciprofloxacin. *Sep. Purif. Technol.* **295**, 121216 (2022).
9. Qiu, B., Shao, Q., Shi, J., Yang, C. & Chu, H. Application of biochar for the adsorption of organic pollutants from wastewater: modification strategies, mechanisms and challenges. *Sep. Purif. Technol.* **300**, 121925 (2022).
10. Li, M. et al. Iron-organic frameworks as effective fenton-like catalysts for peroxymonosulfate decomposition in advanced oxidation processes. *npj Clean Water* **6**, 37 (2023).
11. Saravanakumar, K., Jagan, G., Lee, J., Park, C. M. & MOF-derived, C. N-In$_2$O$_3$ with GdFeO$_3$ Z-scheme heterostructure for the photocatalytic removal of tetracycline. *npj Clean Water* **6**, 72 (2023).
12. Keshta, B. E., Yu, H. & Wang, L. MIL series-based MOFs as effective adsorbents for removing hazardous organic pollutants from water. *Sep. Purif. Technol.* **322**, 124301 (2023).
13. Xia, Q. et al. State-of-the-art advances and challenges of iron-based metal organic frameworks from attractive features, synthesis to multifunctional applications. *Small* **15**, 1803088 (2019).
14. Xu, L., Chen, Y., Su, W., Cui, J. & Wei, S. Synergistic adsorption of U(VI) from seawater by MXene and amidoxime mixed matrix membrane with high efficiency. *Sep. Purif. Technol.* **309**, 123024 (2023).
15. Nguyen, C. H., Fu, C.-C., Kao, D.-Y., Tran, T. T. V. & Juang, R.-S. Adsorption removal of tetracycline from water using poly(vinylidene fluoride)/polyaniline-montmorillonite mixed matrix membranes. *J. Taiwan Inst. Chem. Eng.* **112**, 259–270 (2020).
16. Zeng, H., Wang, L., Zhang, D. & Wang, C. Efficient capture and detoxification of mercury dichloride from wastewater by a PVDF/PEI adsorption membrane. *Chem. Eng. J.* **468**, 143621 (2023).
17. Shen, L. et al. Surface modification of polyvinylidene fluoride (PVDF) membrane via radiation grafting: novel mechanisms underlying the interesting enhanced membrane performance. *Sci. Rep.* **7**, 2721 (2017).
18. Ye, Q. et al. Metal-organic framework modified hydrophilic polyvinylidene fluoride porous membrane for efficient degerming selective oil/water emulsion separation. *npj Clean Water* **5**, 23 (2022).
19. Chandrashekar, A. et al. Non-covalent surface functionalization of nanofillers towards the enhancement of thermal conductivity of polymer nanocomposites: a mini review. *Eur. Polym. J.* **198**, 112379 (2023).
20. Tang, J. et al. Carbodiimide coupling versus click chemistry for nanoparticle surface functionalization: A comparative study for the encapsulation of sodium cholate by cellulose nanocrystals modified with β-cyclodextrin. *Carbohydr. Polym.* **244**, 116512 (2020).
21. Sikder, M. T. et al. Remediation of water pollution with native cyclodextrins and modified cyclodextrins: A comparative overview and perspectives. *Chem. Eng. J.* **355**, 920–941 (2019).
22. Herrera, B. A. et al. A surface functionalized with per-(6-amino-6-deoxy)-β-cyclodextrin for potential organic pollutant removal from water. *Carbohydr. Polym.* **233**, 115865 (2020).
23. Zhao, P. et al. In-situ growth of polyvinylpyrrolidone modified Zr-MOFs thin-film nanocomposite (TFN) for efficient dyes removal. *Compos. B Eng.* **176**, 107208 (2019).
24. Nam, S.-N. et al. Performance assessment and optimization of forward osmosis–low pressure ultrafiltration hybrid system using

25. Iftikhar, S. et al. Artificial neural networks for insights into adsorption capacity of industrial dyes using carbon-based materials. *Sep. Purif. Technol.* **326**, 124891 (2023).

26. Asoubar, S., Mehrizad, A., Behnajady, M. A., Ramazani, M. E. & Gharbani, P. Hexavalent chromium reduction and Rhodamine B degradation by visible-light-driven photocatalyst of stannum indium sulfide-samarium vanadate. *npj Clean Water* **6**, 27 (2023).

27. Ghaedi, A. M. & Vafaei, A. Applications of artificial neural networks for adsorption removal of dyes from aqueous solution: a review. *Adv. Colloid Interface Sci.* **245**, 20–39 (2017).

28. Hou, J. et al. Characteristics and mechanisms of sulfamethoxazole adsorption onto modified biochars with hierarchical pore structures: batch, predictions using artificial neural network and fixed bed column studies. *J. Water Process Eng.* **54**, 103975 (2023).

29. Momina & Ahmad, K. Remediation of anionic dye from aqueous solution through adsorption on polyaniline/FO nanocomposite-modelling by artificial neural network (ANN). *J. Mol. Liq.* **360**, 119497 (2022).

30. Maurya, A. K. et al. Development of artificial neural networks software for arsenic adsorption from an aqueous environment. *Environ. Res.* **203**, 111846 (2022).

31. Qalyoubi, L., Al-Othman, A. & Al-Asheh, S. Removal of ciprofloxacin antibiotic pollutants from wastewater using nano-composite adsorptive membranes. *Environ. Res.* **215**, 114182 (2022).

32. Das, S., Barui, A. & Adak, A. Montmorillonite impregnated electrospun cellulose acetate nanofiber sorptive membrane for ciprofloxacin removal from wastewater. *J. Water Process Eng.* **37**, 101497 (2020).

33. Guo, J. et al. Fouling behavior of negatively charged PVDF membrane in membrane distillation for removal of antibiotics from wastewater. *J. Membr. Sci.* **551**, 12–19 (2018).

34. Bhattacharya, P., Mukherjee, D., Dey, S., Ghosh, S. & Banerjee, S. Development and performance evaluation of a novel CuO/TiO$_2$ ceramic ultrafiltration membrane for ciprofloxacin removal. *Mater. Chem. Phys.* **229**, 106–116 (2019).

35. Baig, N., Abdulazeez, I. & Aljundi, I. H. Low-pressure-driven special wettable graphene oxide-based membrane for efficient separation of water-in-oil emulsions. *npj Clean Water* **6**, 40 (2023).

36. Wang, Q. et al. The strong interaction and confinement effect of Ag@NH2-MIL-88B for improving the conversion and durability of photocatalytic Cr(VI) reduction in the presence of a hole scavenger. *J. Hazard. Mater.* **451**, 131149 (2023).

37. Xie, A. et al. Photo-Fenton self-cleaning PVDF/NH$_2$-MIL-88B(Fe) membranes towards highly-efficient oil/water emulsion separation. *J. Membr. Sci.* **595**, 117499 (2020).

38. Shao, L. et al. Carbon nanodots anchored onto the metal-organic framework NH$_2$-MIL-88B(Fe) as a novel visible light-driven photocatalyst: photocatalytic performance and mechanism investigation. *Appl. Surf. Sci.* **505**, 144616 (2020).

39. Tran, T. V. et al. Hexagonal Fe-based MIL-88B nanocrystals with NH$_2$ functional groups accelerating oxytetracycline capture via hydrogen bonding. *Surf. Interfaces* **20**, 100605 (2020).

40. Corciova, A. et al. Antibacterial and antioxidant properties of hesperidin:β-cyclodextrin complexes obtained by different techniques. *J. Incl. Phenom. Macrocycl. Chem.* **81**, 71–84 (2015).

41. Dehghani, A., Bahlakeh, G. & Ramezanzadeh, B. Beta-cyclodextrin-zinc acetylacetonate (β-CD@ZnA) inclusion complex formation as a sustainable/smart nanocarrier of corrosion inhibitors for a water-based siliconized composite film: Integrated experimental analysis and fundamental computational electronic/atomic-scale simulation. *Compos. B Eng.* **197**, 108152 (2020).

42. Bai, H., Wang, X., Zhou, Y. & Zhang, L. Preparation and characterization of poly(vinylidene fluoride) composite membranes blended with nano-crystalline cellulose. *Prog. Nat. Sci. Mater. Int.* **22**, 250–257 (2012).

43. Ali, H. & Ismail, A. M. Developing montmorillonite/PVDF/PEO microporous membranes for removal of malachite green: adsorption, isotherms, and kinetics. *J. Polym. Res.* **28**, 429 (2021).

44. Nguyen, H.-T. T. et al. Bimetallic Al/Fe metal-organic framework for highly efficient photo-Fenton degradation of rhodamine B under visible light irradiation. *Mater. Lett.* **279**, 128482 (2020).

45. Ramasubramanian, B. et al. Sustainable Fe-MOF@carbon nanocomposite electrode for supercapacitor. *Surf. Interfaces* **34**, 102397 (2022).

46. He, H. et al. Confined conductive and light-adsorbed network in metal organic frameworks (MIL-88B(Fe)) with enhanced photo-Fenton catalytic activity for sulfamethoxazole degradation. *Chem. Eng. J.* **427**, 131962 (2022).

47. Rabeie, B. & Mahmoodi, N. M. Heterogeneous MIL-88A on MIL-88B hybrid: a promising eco-friendly hybrid from green synthesis to dual application (Adsorption and photocatalysis) in tetracycline and dyes removal. *J. Colloid Interface Sci* **654**, 495–522 (2024).

48. Banerjee, A. et al. MOF derived porous carbon–Fe$_3$O$_4$ nanocomposite as a high performance, recyclable environmental superadsorbent. *J. Mater. Chem.* **22**, 19694–19699 (2012).

49. Ma, Y.-X. et al. One-step fabrication of β-cyclodextrin modified magnetic graphene oxide nanohybrids for adsorption of Pb(II), Cu(II) and methylene blue in aqueous solutions. *Appl. Surf. Sci.* **459**, 544–553 (2018).

50. Guo, H., Niu, B., Wu, X., Zhang, Y. & Ying, S. Effective removal of 2,4,6-trinitrophenol over hexagonal metal–organic framework NH$_2$-MIL-88B(Fe). *Appl. Organomet. Chem.* **33**, e4580 (2019).

51. Hu, L., Zhang, Y., Lu, W., Lu, Y. & Hu, H. Easily recyclable photocatalyst Bi$_2$WO$_6$/MOF/PVDF composite film for efficient degradation of aqueous refractory organic pollutants under visible-light irradiation. *J. Mater. Sci.* **54**, 6238–6257 (2019).

52. Gao, Y. et al. A photo-Fenton self-cleaning membrane based on NH$_2$-MIL-88B (Fe) and graphene oxide to improve dye removal performance. *J. Membr. Sci.* **626**, 119192 (2021).

53. Li, Y. et al. TiO$_2$ nanoparticles anchored onto the metal–organic framework NH$_2$-MIL-88B(Fe) as an adsorptive photocatalyst with enhanced Fenton-like degradation of organic pollutants under visible light irradiation. *ACS Sustain. Chem. Eng* **6**, 16186–16197 (2018).

54. Su, Q. et al. Visible-light-driven photocatalytic degradation of ofloxacin by g-C$_3$N$_4$/NH$_2$-MIL-88B(Fe) heterostructure: mechanisms, DFT calculation, degradation pathway and toxicity evolution. *Chem. Eng. J.* **427**, 131594 (2022).

55. Sun, L., Gu, Q. C., Wang, H. L., Yu, J. S. & Zhou, X. G. Anhydrous proton conductivity of electrospun phosphoric acid-doped PVP-PVDF nanofibers and composite membranes containing MOF fillers. *RSC Adv.* **11**, 29527–29536 (2021).

56. Isloor, A. M. et al. Novel polyphenylsulfone (PPSU)/nano tin oxide (SnO$_2$) mixed matrix ultrafiltration hollow fiber membranes: Fabrication, characterization and toxic dyes removal from aqueous solutions. *React. Funct. Polym.* **139**, 170–180 (2019).

57. Liu, F., Hashim, N. A., Liu, Y., Abed, M. R. M. & Li, K. Progress in the production and modification of PVDF membranes. *J. Membr. Sci.* **375**, 1–27 (2011).

58. Chang, X. et al. Exploring the synergetic effects of graphene oxide (GO) and polyvinylpyrrodione (PVP) on poly(vinylylidenefluoride) (PVDF) ultrafiltration membrane performance. *Appl. Surf. Sci.* **316**, 537–548 (2014).

59. Verma, M. et al. Simultaneous removal of heavy metals and ciprofloxacin micropollutants from wastewater using ethylenediaminetetraacetic acid-functionalized β-cyclodextrin-chitosan adsorbent. *ACS Omega* **6**, 34624–34634 (2021).

60. Yadav, S. et al. Adsorption of cationic dyes, drugs and metal from aqueous solutions using a polymer composite of magnetic/β-cyclodextrin/activated charcoal/Na alginate: isotherm kinetics and regeneration studies. *J. Hazard. Mater.* **409**, 124840 (2021).

61. Peng, X. et al. Preparation of a graphitic ordered mesoporous carbon and its application in sorption of ciprofloxacin: kinetics, isotherm, adsorption mechanisms studies. *Microporous Mesoporous Mater.* **228**, 196–206 (2016).

62. Chandrasekaran, A., Patra, C., Narayanasamy, S. & Subbiah, S. Adsorptive removal of ciprofloxacin and amoxicillin from single and binary aqueous systems using acid-activated carbon from Prosopis juliflora. *Environ. Res.* **188**, 109825 (2020).

63. Lv, M. et al. Effects of heavy metals on the adsorption of ciprofloxacin on polyethylene microplastics: mechanism and toxicity evaluation. *Chemosphere* **315**, 137745 (2023).

64. Gu, J. et al. New insight into adsorption and co-adsorption of chlortetracycline hydrochloride and ciprofloxacin hydrochloride by Ga-based metal-organic gel/sodium alginate composite beads. *Sep. Purif. Technol.* **312**, 123408 (2023).

65. Ma, Y. et al. Hydrothermal synthesis of magnetic sludge biochar for tetracycline and ciprofloxacin adsorptive removal. *Bioresour. Technol.* **319**, 124199 (2021).

66. Yang, C., Zhang, J., Yan, W. & Xia, Y. Facile synthesis of hierarchical porous MOFs via competition coordination strategy: A sustainable adsorbent for efficient removal of fluorine-containing drugs. *Sep. Purif. Technol.* **320**, 124111 (2023).

67. Atugoda, T., Gunawardane, C., Ahmad, M. & Vithanage, M. Mechanistic interaction of ciprofloxacin on zeolite modified seaweed (Sargassum crassifolium) derived biochar: kinetics, isotherm and thermodynamics. *Chemosphere* **281**, 130676 (2021).

68. Kim, N. et al. Effective sequestration of tetracycline and ciprofloxacin from aqueous solutions by Al-based metal organic framework and reduced graphene oxide immobilized alginate biosorbents. *Chem. Eng. J.* **450**, 138068 (2022).

69. Bazgir, S., Farhadi, S. & Mansourpanah, Y. Adsorptive removal of tetracycline and ciprofloxacin antibiotics from water using magnetic MIL101-Fe metal–organic framework/NiFe$_2$O$_4$ decorated with Preyssler-Pope-Jeannin [NaP5W30O110]$^{14-}$ polyanion. *J. Solid State Chem.* **315**, 123513 (2022).

70. Aytac, Z., Ipek, S., Erol, I., Durgun, E. & Uyar, T. Fast-dissolving electrospun gelatin nanofibers encapsulating ciprofloxacin/cyclodextrin inclusion complex. *Colloids Surf. B* **178**, 129–136 (2019).

Author contributions
L.K.N.: conceptualization, methodology, software, visualization, calculation, and writing—original draft. Y.Y.: supervision; validation; visualization, and formal analysis. C.P.: conceptualization, writing—review and editing, supervision, funding acquisition, and validation.

Competing interests
The authors declare no competing interests.

Additional information
Supplementary information The online version contains supplementary material available at https://doi.org/10.1038/s41545-024-00312-x.

Correspondence and requests for materials should be addressed to Chang Min Park.

Reprints and permissions information is available at http://www.nature.com/reprints

Publisher's note Springer Nature remains neutral with regard to jurisdictional claims in published maps and institutional affiliations.